Journal of Advanced Ceramics
2022, **11**(8): 1294–1306
https://doi.org/10.1007/s40145-022-0610-6
ISSN 2226-4108
CN 10-1154/TQ

Research Article

Experimental and DFT studies of flower-like Ni-doped Mo_2C on carbon fiber paper: A highly efficient and robust HER electrocatalyst modulated by $Ni(NO_3)_2$ concentration

Lei ZHANG[a,†], Zhihui HU[a,†], Juntong HUANG[a,*], Zhi CHEN[a], Xibao LI[a], Zhijun FENG[a], Huiyong YANG[a], Saifang HUANG[b,*], Ruiying LUO[a,c,*]

[a]*School of Materials Science and Engineering*, *Nanchang Hangkong University*, *Nanchang 330063*, *China*
[b]*School of Materials Science and Engineering*, *Jiangsu University of Science and Technology*, *Zhenjiang 212003*, *China*
[c]*Research Institute for Frontier Science*, *Beihang University*, *Beijing 100191*, *China*

Received: January 11, 2022; Revised: May 3, 2022; Accepted: May 7, 2022

Abstract: Developing highly efficient and stable non-precious metal catalysts for water splitting is urgently required. In this work, we report a facile one-step molten salt method for the preparation of self-supporting Ni-doped Mo_2C on carbon fiber paper (Ni–Mo_2C_{CB}/CFP) for hydrogen evolution reaction (HER). The effects of nickel nitrate concentration on the phase composition, morphology, and electrocatalytic HER performance of Ni-doped Mo_2C@CFP electrocatalysts was investigated. With the continuous increase of $Ni(NO_3)_2$ concentration, the morphology of Mo_2C gradually changes from granular to flower-like, providing larger specific surface area and more active sites. Doping nickel (Ni) into the crystal lattice of Mo_2C largely reduces the impedance of the electrocatalysts and enhances their electrocatalytic activity. The as-developed Mo_2C–3 M $Ni(NO_3)_2$/CFP electrocatalyst exhibits high catalytic activity with a small overpotential of 56 mV at a current density of 10 $mA \cdot cm^{-2}$. This catalyst has a fast HER kinetics, as demonstrated by a very small Tafel slope of 27.4 $mV \cdot dec^{-1}$, and persistent long-term stability. A further higher Ni concentration had an adverse effect on the electrocatalytic performance. Density functional theory (DFT) calculations further verified the experimental results. Ni doping could reduce the binding energy of Mo–H, facilitating the desorption of the adsorbed hydrogen (H_{ads}) on the surface, thereby improving the intrinsic catalytic activity of Ni-doped Mo_2C-based catalysts. Nevertheless, excessive Ni doping would inhibit the catalytic activity of the electrocatalysts. This work not only provides a simple strategy for the facile preparation of non-precious metal electrocatalysts with high catalytic activity, but also unveils the influence mechanism of the Ni doping concentration on the HER performance of the electrocatalysts from the theoretical perspective.

† Lei Zhang and Zhihui Hu contributed equally to this work.
* Corresponding authors.
E-mail: J. Huang, huangjt@nchu.edu.cn;
S. Huang, s.huang@just.edu.cn;
R. Luo, ryluo@buaa.edu.cn

Keywords: Mo_2C@CFP electrocatalyst; nickel (Ni) doping; hydrogen evolution reaction (HER); water splitting; molten salt method

1 Introduction

Fossil fuels have been utilized for many centuries to support the fast development of modern society, with rapidly decreased reserves on the Earth as they are non-renewable sources. Nevertheless, they are notoriously known as dirty energy sources, which give out emissions and air pollutants as a consequence of combustion, causing many challenges such as air pollution and global warming. Thus, seeking for clean and renewable energy alternatives to fossil fuels is utmost urgent across the world. It is widely known that hydrogen is deemed as an ideal energy carrier, which serves as a perfect alternative to fossil fuels owing to its environmental friendliness and high energy density features [1]. Water splitting is a very promising technique for hydrogen generation, which gives out hydrogen via the hydrogen evolution reaction (HER) enabled by photocatalysts [2–4], electrocatalysts, or photoelectrocatalysts [5,6], where solar energy can be utilized directly or indirectly [7,8]. To enable practical applications in water splitting, it is essential to develop highly active, efficient, and robust electrocatalysts from economical resources [9,10]. Generally, noble metal- (e.g., Pt- [11], Ru- [12], and Ir- [13]) based catalysts have superior catalytic performance for HER, while their scarcity in the earth crust makes them very costly, thereby hampering its practical applications in large scale. In this context, noble metal-free catalysts for water splitting [14,15] have attracted increasing attentions, which include but not limited to earth-abundant carbon-based and transition-metal-based electrocatalysts [16,17].

The transition-metal-based compounds such as chalcogenides, phosphides, nitrides, and carbides have been investigated for electrochemical hydrogen evolution. Among them, transition-metal carbides (TMCs) known for their high corrosion resistance and chemical and mechanical stability, such as WC [18], TaC [19], and Mo_2C [20–23], have demonstrated excellent electrochemical catalytic performance. They have unique electronic conductivity in various electrolyte mediums with a broad range of pH values. With similar d-band electronic structure to Pt-group metals, molybdenum carbide (Mo_2C) is a promising electrocatalyst candidate. Its carbon atoms occupy the interstitial positions aside molybdenum atoms, allowing that it has higher d-band electronic density of states (DOS) at the Fermi level [24]. Unfortunately, Mo_2C alone can hardly replace Pt-based electrocatalysts due to its poor conductivity, slow interfacial reaction kinetics, and high onset potentials [25]. Also, the hydrogen binding energy (HBE) between Mo and H is too strong according to the volcano diagram, making it hard to desorb hydrogen, while it is relatively weak between nickel (Ni) and H [26]. Therefore, it is possible to control the Mo_2C-based electrocatalysts with satisfying HBE between Mo and H by adding Ni dopants. The synergic effect between Ni and Mo is beneficial for balancing hydrogen adsorption and desorption, thus improving the HER kinetics and electrocatalytic activity and further achieving highly efficient water splitting.

To date, many approaches have been put forward for enhancing the catalytic activity of Mo_2C-based electrocatalysts [27–29]. One strategy is to increase the specific surface area for exposing more active sites through morphology design [30,31], reducing particle size [32,33], and creating pore structures [34,35]. An alternative strategy is to enhance the electron transfer rate by tailoring electronic configuration via heteroatom doping [36,37]. In addition, dopants such as Ni can reduce the HBE of active sites in the catalysts [38,39]. In Ref. [40], we developed a scalable route upon the molten salt method for the synthesis of a Mo_2C-based electrocatalyst with wrinkled nanotexture, i.e., Ni-doped Mo_2C on carbon fiber paper (Ni–Mo_2C_{CB}/CFP) from Ni, Mo, and carbon black (CB). Ni doping significantly improved its electrocatalytic performance, exhibiting an overpotential of 121.4 mV to achieve a current density of 10 $mA \cdot cm^{-2}$ in acidic medium and long term durability. However, only one sample with Ni doping was studied. It is of great interest to further investigate the effect of Ni contents on the phase composition, morphology, and electrochemical property of Mo_2C electrocatalysts.

CFP is considered as an ideal carbon-based material for supporting electrocatalysts ascribing to its merits such as high conductivity, high mechanical strength, and low cost. In this work, we adopted the molten salt

method to fabricate the electrocatalysts of flower-like Mo_2C *in-situ* growing on a CFP that was pre-soaked in nickel nitrate solution with a variety of concentrations (x), denoted as Mo_2C–xNi$(NO_3)_2$/CFP. The influence of Ni content (in the form of concentration of nickel nitrate) on their phase composition, morphology, elemental distribution, and electrocatalytic HER performance was evaluated. The optimal Mo_2C–3 M Ni$(NO_3)_2$/CFP electrocatalyst showed small overpotential of 56 mV (at a current density of 10 mA·cm^{-2}) and remarkable long-term stability. Density functional theory (DFT) calculations were performed to calculate the HBE on the surface Mo_2C doped with different Ni concentrations. The mechanism for the enhancement of electrocatalytic performance was discussed. Based on the DFT calculations and experimental characterizations, it is found that controlling the Ni doping content can affect the synergy between Ni and Mo atoms, and also optimize the binding energy between the surface of active sites and hydrogen atoms, which is expected to facilitate an efficient HER process.

2 Experimental

2. 1 Material preparation

The main raw materials were CFP (TGH-060, Toray Industries, Inc.), CB (99.9% purity, < 100 nm, Beijing Deke Daojin Science and Technology Co., Ltd.), MoO_3 (99.95% purity, Shanghai Macklin Biochemical Co., Ltd.), and Ni$(NO_3)_2$·6H_2O (98% purity, Shanghai Macklin Biochemical Co., Ltd.). A mixture of NaCl and KCl (both with 99.5% purity, Shanghai Macklin Biochemical Co., Ltd.) were used as the molten salt.

For the synthesis of Mo_2C–xNi$(NO_3)_2$/CFP (x = 0.5–4 M), nickel nitrate solution with different concentrations were first prepared by weighing Ni$(NO_3)_2$·6H_2O in different amounts (5, 10, 15, 20, 25, 30, 35, and 40 mmol), which were dissolved in 10 mL distilled water. In a typical synthesis process, CFP (15 mm × 10 mm, with a thickness of ca. 0.33 mm and weight of 33.6 mg) was treated by sonication in alcohol, 0.1 M H_2SO_4, and distilled water in sequence, for 10 min each, to remove the surface cement and dried subsequently. The pretreated CFP was then soaked in the as-prepared nickel nitrate solution for 20 h to allow it being completely moistened. The CFP was not only used as a substrate, but also a carbon source for the synthesis of Mo_2C–xNi$(NO_3)_2$/CFP electrocatalysts. The CFP loaded with nickel nitrate was placed in a crucible with well-mixed MoO_3 (115.2 mg), CB (33.6 mg), and salts (20 g) consisting of equimolar NaCl and KCl. The crucible was then placed in a tube furnace and heat-treated at 1000 ℃ for 6 h under a flowing argon atmosphere, and allowed to cool down to room temperature. The product was repeatedly washed in hot distilled water to rinse out the remaining salt. As a control, the pre-treated CFP without loading nickel nitrate solution was utilized to synthesize Ni-free Mo_2C by following the identical protocol (labeled as Mo_2C/CFP).

2. 2 Material characterizations

The phase compositions were identified by using an X-ray diffractometer with Cu Kα radiation (D8 Advance A25, Bruker AXS, Germany). The chemical compositions and elemental mappings of the catalysts were analyzed by the energy dispersive X-ray spectroscope (EDS; INCA 250 X-Max 50, Oxford Instrument, UK). The morphologies and microstructures of the catalysts were observed with the field emission scanning electron microscope (FE-SEM; Nova Nano SEM450, FEI, USA) and the field emission transmission electron microscope (FE-TEM; TalosF200X, FEI, USA). The surface elemental compositions and valence states of the catalysts were obtained by the X-ray photoelectron spectroscopy (XPS) using an electron spectrometer (Axis Ultra DLD, Shimadza-Kratos, USA) with Al Kα radiation operated at 150 W, and the elemental peak fitting was performed via the CasaXPS software (Casa Software Ltd., UK). The loadings of all the catalysts on the CFP were examined with a high-precision analytical balance (AR224CN, 0.1 mg, Ohaus, China).

2. 3 Preparation of the 20% Pt/C electrode

To prepare the 20% Pt/C electrode, 2 mg commercial 20% Pt/C catalyst was dispersed in a 2 mL mixture of ethanol and 5% Nafion (8:1 *V*/*V*), followed by the sonication to form a homogeneous ink. Afterward, the well-dispersed catalyst was coated on a CFP (10 mm × 10 mm) with a mass loading of 0.6 mg·cm^{-2}. The 20% Pt/C catalyst was then dried at room temperature for further measurements.

2. 4 Electrochemical measurements

The electrochemical performance of the electrocatalysts was tested in a 0.5 M H_2SO_4 electrolyte at 25 ℃ on an

electrochemical workstation (CHI760E, CH Instruments, Inc., China) with a conventional three-electrode system, where a standard Ag/AgCl electrode was used as the reference electrode, Pt plate (20 mm × 20 mm) as the counter electrode, and the as-prepared electrodes as the working electrode. The as-prepared electrodes were defined to an area of 10 mm × 10 mm by an electrochemically inert silicon rubber.

All potentials were referenced to the reversible hydrogen electrode (RHE) ($E_{RHE} = E_{Ag/AgCl} + 0.199$ V + 0.059 × pH). The linear sweep voltammetry (LSV) polarization curves were recorded at a scan rate of 2 mV·s^{-1}. The electrochemical impedance spectroscopy (EIS) measurements were performed from 100 kHz to 0.1 Hz at an overpotential of −100 mV. Chronoamperometry measurements were performed at the current density of −10 mA·cm^{-2} for 35 h. Continuous cyclic voltammetry (CV) was performed between −0.2 and 0.2 V at a scan rate of 100 mV·s^{-1}. To estimate the electrochemical active surface area (ECSA) of the catalysts, CV was tested within the non-Faraday potential range (0.1–0.22 V vs. RHE) at various scan rates (20, 40, 60, 80, and 100 mV·s^{-1}). All the collected data were corrected for *IR* compensation, unless otherwise stated.

2. 5 DFT calculations

DFT calculations were performed using the Vienna *Ab-initio* Simulation Package (VASP) code [41–43]. For the total energy calculations, the plane wave cutoff energy was 400 eV. Ion–electron interactions were represented by ultrasoft pseudopotentials within the framework of the projector-augmented wave (PAW) method [44]. The generalized gradient approximation (GGA) with the Perdew–Burke–Ernzerhof (PBE) functional was adopted as the exchange-correlation functional [45]. DFT-D2 was utilized to correct the van der Waals interactions between molecules while maintaining an accurate chemisorption energy. The Brillouin zone integration was approximated by a sum over specially-selected *k*-points using the 2×2×1 Monkhorst–Pack method [46]. The geometries were optimized until the energy was converged to 5×10^{-5} eV/atom, and the forces was converged to 0.02 eV/Å.

The calculation of the free energy was performed by using the concept of computational hydrogen electrode (CHE). The change of the free energy (ΔG_{H*}) can be calculated by Eq. (1):

$$\Delta G_{H*} = \Delta E + \Delta ZPE - T\Delta S \quad (1)$$

where ΔE is the energy directly obtained by DFT calculations, ΔZPE is the change in zero-point energies (ZPE), T (= 298.15 K) is the room temperature, and ΔS is the entropy change. The ZPE and vibrational entropy of the adsorbed species were obtained after frequency calculations.

For Mo_2C crystal, the $p(3\times4)$–(101) surface was considered in this study, and modeled using three Mo–C–Mo layers. During the calculations, the bottom layer of Mo was fixed, and other layers and the adsorbed species were relaxed. Moreover, in order to eliminate the interactions between slabs, the vacuum region was set to 15 Å in the z direction to separate the slabs.

3 Results and discussion

3. 1 Phase, microstructural, and chemical analyses

The X-ray diffraction (XRD) patterns of Mo_2C/CFP and Mo_2C–xNi$(NO_3)_2$/CFP synthesized via the molten salt method are shown in Fig. 1. Mo_2C–xNi$(NO_3)_2$/CFP electrocatalysts present obvious diffraction peaks of Mo_2C (JCPDS Card No. 35-0787), Ni (JCPDS Card No. 04-0850), and carbon (JCPDS Card No. 41-1487). As seen from the patterns, the peak intensities of Mo_2C and Ni phases gradually increase with the rise of nickel nitrate concentration. In addition, as seen from the

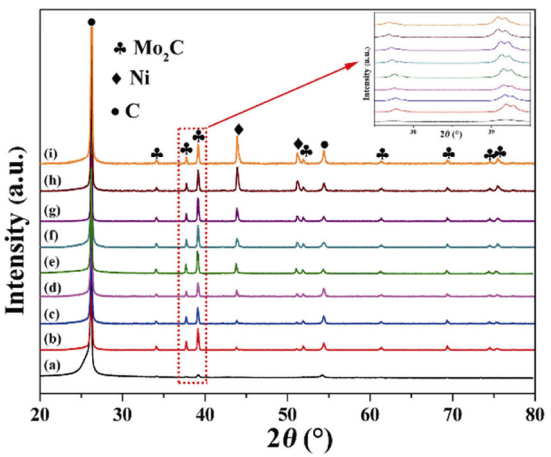

Fig. 1 XRD patterns of (a) Mo_2C/CFP, (b) Mo_2C–0.5 M Ni$(NO_3)_2$/CFP, (c) Mo_2C–1 M Ni$(NO_3)_2$/CFP, (d) Mo_2C–1.5 M Ni$(NO_3)_2$/CFP, (e) Mo_2C–2 M Ni$(NO_3)_2$/CFP, (f) Mo_2C–2.5 M Ni$(NO_3)_2$/CFP, (g) Mo_2C–3 M Ni$(NO_3)_2$/CFP, (h) Mo_2C–3.5 M Ni$(NO_3)_2$/CFP, and (i) Mo_2C–4 M Ni$(NO_3)_2$/CFP electrocatalysts. The inset is the corresponding zoom-in regions.

local-enlarged XRD patterns, compared to those of the bare Mo_2C (Fig. 1(a)), the diffraction peaks of Mo_2C displayed a slight shift to a higher diffraction angle, which can be ascribed to the shrinkage of the lattice spacing of Mo_2C when Mo^{2+} in the lattice structure of Mo_2C is replaced by a smaller Ni^{2+} ion. However, some Mo_2C diffraction peaks gradually moved toward a lower angle with an increase in the amount of doped Ni, which might be due to some Ni atoms entering the interstitial position of Mo_2C crystal structure, resulting in the increase of unit cell volume and crystal plane spacing of Mo_2C. It indicates that Ni ions or atoms were likely doped into the lattice of Mo_2C, and Ni doping promoted the formation of Mo_2C.

To examine the influence of concentrations of nickel nitrate solution, the morphology changes of Mo_2C-based electrocatalysts before and after Ni doping were observed by the SEM, and the images are illustrated in Fig. 2. The CFP substrate in all the samples maintained intact after the synthesis of electrocatalysts via the molten salt method. Without Ni doping, micro-sized granular Mo_2C wrapped the carbon fibers (Fig. 2(a)). While by gradually increasing the concentration of $Ni(NO_3)_2$, the evolution of morphology of Mo_2C from granular to flower-like was observed (Figs. 2(b)–2(h)). It suggests that a higher doping concentration of Ni could promote the formation of nanostructured flower-like Mo_2C. Such a morphology has high specific surface area and is beneficial for the electrocatalytic performance (discussed later), providing more active sites compared with the bare Mo_2C/CFP. To be detailed, when x was low (0.5 M, Fig. 2(b)), the granular morphology remained with sporadic flakes formed on the surface of Mo_2C. As Ni concentration (x) increased, tiny nanoflowers formed (x = 1 M) and gradually became larger and defined when x further increased. However, when the doping concentration is higher than 3 M, Ni aggregated and formed bulky grains on the surface of the electrocatalyst (Fig. S1 in the Electronic Supplementary Material (ESM)).

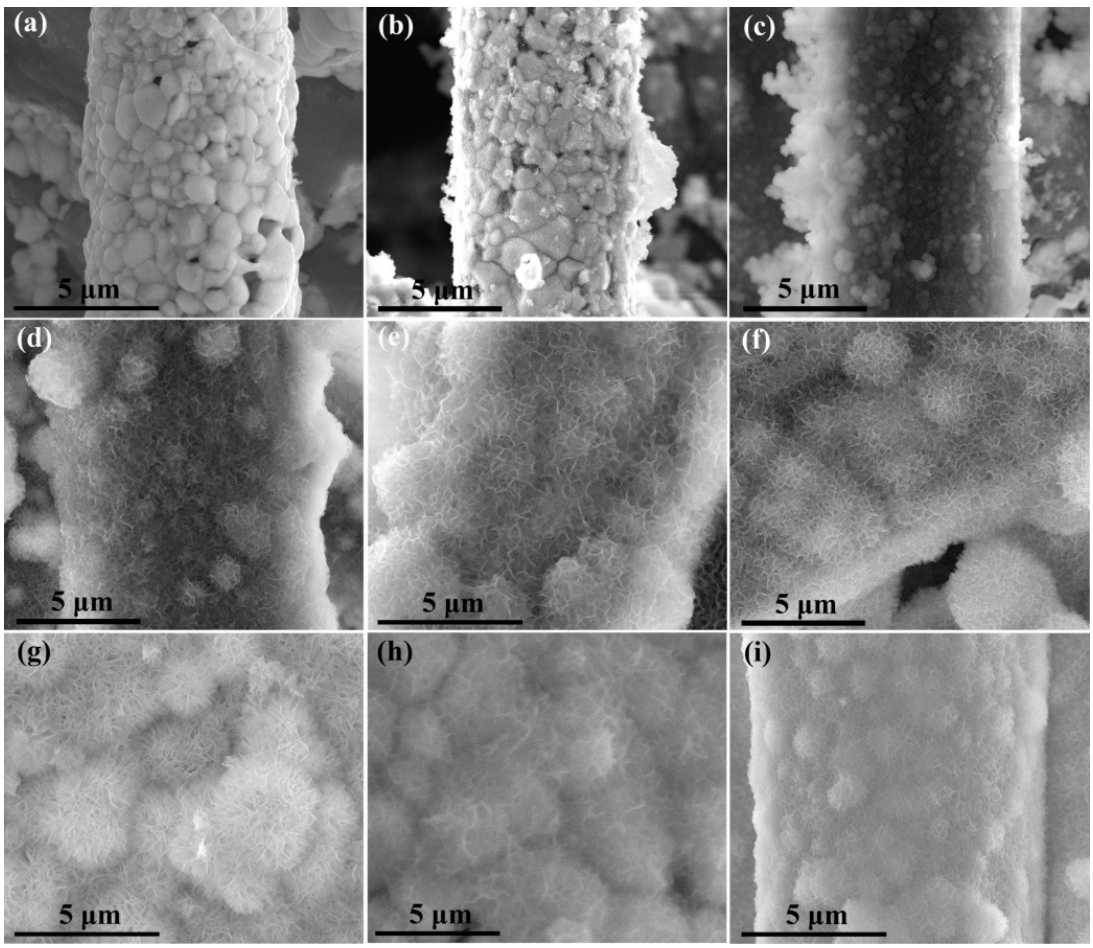

Fig. 2 SEM images of (a) Mo_2C/CFP and (b–i) Mo_2C–xNi$(NO_3)_2$/CFP electrocatalysts: x = (b) 0.5 M, (c) 1 M, (d) 1.5 M, (e) 2 M, (f) 2.5 M, (g) 3 M, (h) 3.5 M, and (i) 4 M.

Flower-like Mo_2C clusters in Mo_2C–3 M $Ni(NO_3)_2$/CFP, which exhibits the best electrocatalytic performance as discussed later, were further observed by the TEM. The nanoflowers are composed of a large number of fluffy nanosheets, as observed in Fig. 3(b). In the high-resolution TEM (HRTEM) images (Fig. 3(c)), the lattice fringes with spacings of 0.23 and 0.2 nm can be clearly observed, corresponding to the (101) crystal plane of Mo_2C and the (111) crystal plane of Ni, respectively. The results obtained by the selected area electron diffraction (SAED) illustrate the diffraction ring of β-Mo_2C and Ni, in good agreement with the XRD results. The high-angle annular dark-field scanning TEM (HAADF-STEM) and corresponding EDS elemental mapping images proved that Mo, Ni, and C elements were uniformly distributed in the whole electrocatalyst. The O element was detected, which may originate from the oxidation of nanostructured Ni metal and/or Mo_2C, forming a very thin layer of oxide coating on its exposed surface. The HRTEM images, ring-type SAED pattern, and EDS mapping results (Figs. 3(c) and 3(d)) evidently suggest that the flower flakes are composed of Ni and Mo_2C, which distributed adjacently and formed multicrystalline domains. Such a microstructural feature would facilitate the electron exchange between Ni and Mo_2C, and lead to the synergic effect on the electrocatalytic performance of the electrocatalyst [47]. In addition, Ni doping caused lattice distortion on Mo_2C, which is beneficial for forming more active sites [48–50].

The chemical states and elemental compositions on the surface of prepared electrocatalysts were further investigated by the XPS. In the C 1s spectra (Fig. S2 in the ESM), the main peaks deconvoluted at 284.8, 283.8, 286.1, and 288.1 eV were corresponding to the C–C, C–Mo, C–O, and O–C–O bonds [51], respectively. This confirmed the oxidation of carbides on the surface. The oxidation also reflected in the Ni peaks (Fig. 4(b)), as discussed in the following. To be specific, apart from the characteristic peaks for metallic Ni^0 at 853.2 and 870.6 eV, Ni^{2+} peaks located at 856.8 and 874.6 eV can be observed. Additionally, characteristic states of Mo^{2+}, Mo^{4+}, and Mo^{6+} can be assigned to the peaks of Mo 3d (Fig. 4(a) and Table S1 in the ESM). Among them, Mo^{4+} and Mo^{6+} originate from the oxidized Mo components [52], while Mo^{2+} can be attributed to the C–Mo bond. The peaks of Mo_2C–xNi$(NO_3)_2$/CFP (x = 1, 2, 3, and 4 M) for Mo 3d obviously shifted toward lower binding energy if compared to those of the bare Mo_2C/CFP while the Ni 2p peaks moved conversely. This electron transfer process helps to form a synergic effect between Ni and Mo_2C, in which Ni with rich electrons acts as an electron donor, and Mo acts as an electron acceptor because of its empty d electron orbital. From the results, we can clearly observe that the peaks of Mo^{2+} at lower binding energy gradually intensify with the increase of Ni concentration. This manifests that Ni doping significantly enhanced the stability of Mo_2C. Besides, the electron density in Mo_2C also increased, which can

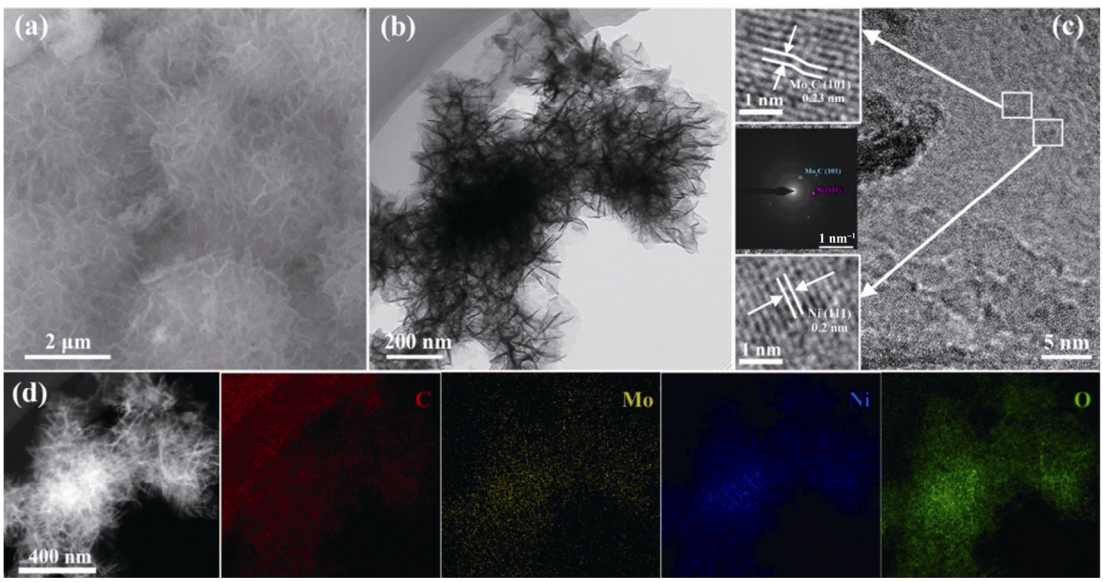

Fig. 3 (a, b) TEM images of Mo_2C–3 M $Ni(NO_3)_2$/CFP, (c) HRTEM images of Mo_2C–3 M $Ni(NO_3)_2$/CFP and the corresponding SAED pattern, and (d) EDS mapping results of C, Mo, Ni, and O in Mo_2C–3 M $Ni(NO_3)_2$/CFP.

weaken the HBE between Mo and H. This promotes the desorption of hydrogen from the electrocatalyst surface, so as to enhance the HER process [53]. Furthermore, as the concentration of $Ni(NO_3)_2$ continued to rise, the peaks for Mo 3d gradually moved to lower binding energy until x reached 3 M, and after that, they moved toward the opposite direction, while the peaks of Ni 2p exhibited a completely opposite shifting process. These results imply that the electron donation from Ni to Mo_2C becomes stronger when the contribution of $Ni(NO_3)_2$ consecutively rises to 3 M, then getting weaker afterwards.

3. 2 Growth mechanism

With the results observed in Fig. 2, a possible mechanism is proposed for the formation of the flower-like Mo_2C–xNi$(NO_3)_2$/CFP on CFP via the molten salt method, and a schematic diagram is illustrated in Fig. 5. Without introducing nickel nitrate on the CFP, MoO_3 was carbonized by CB, forming granular Mo_2C clusters on the CFP substrate and CO gas via Reaction (2). When nickel nitrate was applied on the CFP, it decomposed to nickel oxide (NiO) via Reaction (3), which is readily reduced to Ni by CO in the molten salt system (Reaction (4)). Due to the co-existence of Mo^{2+} and Ni^{2+} ions, both of them refined the microstructure of the product, forming nanoflowers with ultrathin nanosheets on the substrate.

$$2MoO_3 + 7C \rightarrow Mo_2C + 6CO \quad (2)$$

$$Ni(NO_3)_2{\cdot}6H_2O \rightarrow NiO + 2NO_2 + 1/2O_2 + 6H_2O \quad (3)$$

$$NiO + CO \rightarrow Ni + CO_2 \quad (4)$$

In this work, the granular and flower-like morphology of Mo_2C formed before and after Ni doping can be well explained by the crystal structure and formation kinetics of Mo_2C. In the samples without Ni doping, a large number of Mo_2C nuclei formed and grew into granular particles. The Ni doping would slow down the axial growth rate of Mo_2C and increase the radial growth rate. As such, Mo_2C is confined to form a nanosheet structure with Ni homogenously distributed. The nanosheets wrapped on the nuclei, forming three-dimensional nano flower-like structures with the help of directional aggregation [54].

3. 3 Electrocatalytic performance

To investigate the catalytic activity of Mo_2C–xNi$(NO_3)_2$/CFP electrocatalysts for HER, the LSV measurements in acidic medium (0.5 M H_2SO_4) at room temperature were performed, and the results are plotted in Fig. 6(a). For better comparison, the LSV curves of the bare CFP, Mo_2C/CFP, and commercial 20% Pt/C were also tested under the same condition. All the reported overpotentials are referenced to the RHE. Mo_2C/CFP possessed an acceptable electrocatalytic performance (η_{10}) (overpotential at the current density (j) = 10 mA·cm^{-2}) of 308 mV compared to the bare CFP, which exhibited ignorable HER activity. With CFP pre-soaked in the

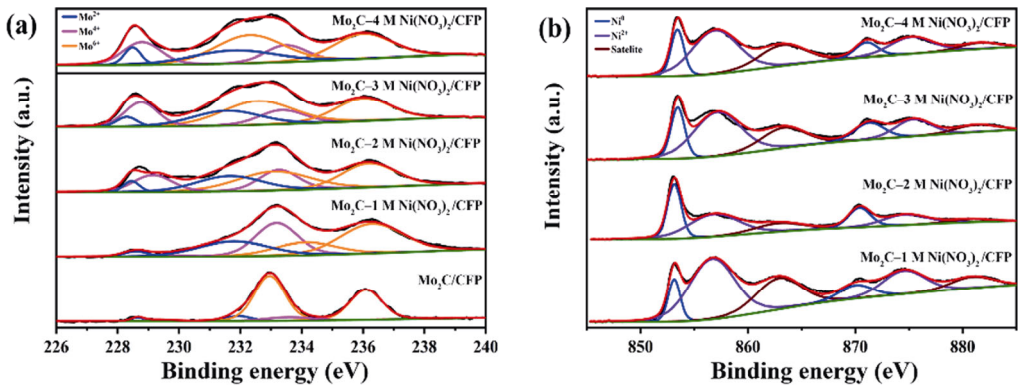

Fig. 4 XPS spectra of Mo_2C–xNi$(NO_3)_2$/CFP: (a) Mo 3d and (b) Ni 2p.

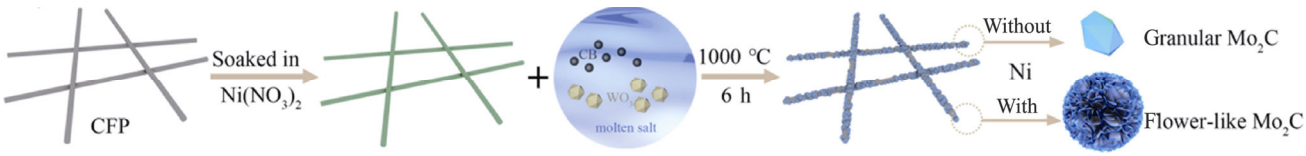

Fig. 5 Scheme of the synthesis process of Mo_2C–3 M $Ni(NO_3)_2$/CFP nanoflower.

nickel nitrate solutions with increasing x, the η_{10} of Mo_2C–xNi$(NO_3)_2$/CFP reduced gradually, that is 202, 167, 130, 100, 73, 56, 135, and 156 mV for x = 0.5, 1, 1.5, 2, 2.5, 3, 3.5, and 4 M, respectively. It can be clearly seen that Ni doping to Mo_2C leads to significant enhancement to the electrocatalytic performance of the Mo_2C/CFP-based catalysts. When x = 3 M, the η_{10} of Mo_2C–xNi$(NO_3)_2$/CFP (56 mV) is comparable to that of commercial 20% Pt/C (48 mV). By tailoring the Ni concentration, the chemical stability of Mo_2C was significantly improved as evidenced by the XPS results in Section 3.1. Moreover, the LSV results demonstrate that the synergic effect between Ni and Mo_2C can be enhanced by optimizing Ni doping concentration, leading to superior electrocatalytic activity that comparable to commercial Pt-based catalysts. However, excessive Ni doping has an adverse effect on the electrocatalytic performance.

Reaction kinetics for HER of the catalysts was further probed by Tafel slopes (Fig. 6(b)). In the acidic medium, HER occurred in the following three steps: Volmer, Heyrovsky, and Tafel reactions [55]. The first step is Volmer reaction that the adsorbed hydrogen (H_{ads}) formed on the surface of catalysts through the adsorption of hydrogen atoms. The subsequent step is either Heyrovsky reaction (desorption step) or Tafel reaction (combination step). It is generally believed that for an electrocatalyst with a Tafel slope of 120, 30, or 40 mV·dec^{-1}, the rate-determine step is Volmer reaction, Heyrovsky reaction, or Tafel reaction, respectively. In this work, the Tafel slope of Mo_2C–3 M Ni$(NO_3)_2$/CFP is 27.4 mV·dec^{-1}, suggesting that HER occurs in a Volmer–Heyrovsky mechanism with Heyrovsky reaction being the rate-determine step. It is also notable that Mo_2C–3 M Ni$(NO_3)_2$/CFP catalysts possess the smallest Tafel slope among all the Mo_2C–xNi$(NO_3)_2$/CFP catalysts (Table 1), comparable to that of the 20% Pt/C (25.8 mV·dec^{-1}). Such a superior performance manifests the great potential of the as-developed electrocatalysts for the pratical application toward HER (Table 2). The small Tafel slope of Mo_2C–3 M Ni$(NO_3)_2$/CFP could be ascribed to several facts. Firstly, the flower-like morphology provides numerous active sites and fast kinetics for hydrogen evolution. Secondly, by increasing the content of Ni in the catalysts, it promotes the electron transfer during HER process, and boosts the synergic effect between Ni and Mo_2C. Thirdly, Ni doping in the lattice of Mo_2C can also lower down the HBE of active sites in the catalysts, promoting the desorption of hydrogen from

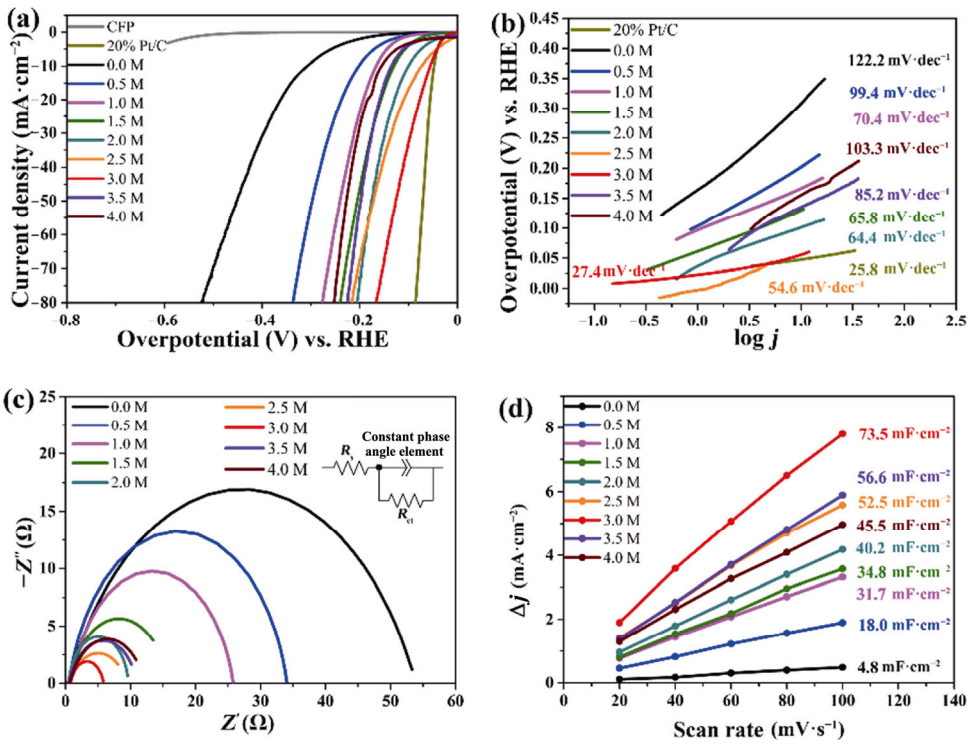

Fig. 6 HER measurements in 0.5 M H_2SO_4: (a) HER polarization curves for different electrocatalysts at a scan rate of 2 mV·s^{-1}; (b) Tafel plots; (c) EIS Nyquist plots for the as-prepared samples obtained at −100 mV (the inset shows the equivalent circuit model); and (d) capacitive currents at different scan rates.

Table 1 Kinetic parameters of Mo_2C–xNi$(NO_3)_2$/CFP electrocatalysts for HER in a 0.5 M H_2SO_4 solution

Catalyst x (M)	η_{10} (mV)	Tafel slope (mV·dec^{-1})	R_{ct} (Ω)	C_{dl} (mF·cm^{-2})	Catalyst x (M)	η_{10} (mV)	Tafel slope (mV·dec^{-1})	R_{ct} (Ω)	C_{dl} (mF·cm^{-2})
0	308	122.2	53.2	4.8	2.5	73	54.6	8.7	52.5
0.5	202	99.4	34.6	18.0	3.0	56	27.4	5	73.5
1.0	167	70.4	25.6	31.7	3.5	135	85.2	10.5	56.6
1.5	130	65.8	15.4	34.8	4.0	156	103.3	11.6	45.5
2.0	100	64.4	9.3	40.2					

Table 2 Comparison of the HER performance for Mo_2C–3 M Ni$(NO_3)_2$/CFP catalyst with other Mo-based electrocatalysts or carbides tested in 0.5 M H_2SO_4 electrolyte

Catalyst	Loading (mg·cm^{-2})	Synthesize method	η_{10} (mV)	Tafel slope (mV·dec^{-1})	Ref.
Mo_2C–3 M Ni$(NO_3)_2$/CFP	2.0	Molten salt method	56	27.4	This work
HMCNB	0.428	One-pot pyrolysis method	143	49.6	[56]
Mo_2C-132/NrGO-30	0.2	Template method	62	59	[57]
N,P–MO_xC NF	0.265	Interfacial polymerization method	107	57.1	[58]
Mo_2C/C hybrid	0.6	High-temperature treatment method	146	60	[59]
Mo_2C NWAs/CFP	2.2	Template method	190	68	[60]
MoP NWs/CFP	2.8	Template method	96	62	[60]
P–Mo_2C@C	1.30	Pyrolysis method	89	42	[61]
mPF/Co–MoS_2	1	Wet impregnation method	156	74	[62]
N–Mo_2C@CNT	0.24	Solvothermal method	183	73.95	[63]
Mo_2N–Mo_2C/HGr-3	0.337	*In-situ* catalytic etching method	157	55	[64]
$MoSe_2$/graphene/NF	5	Solution bath method	92	42	[65]
Mo–Mo_2C-0.077	0.38	Solvothermal method	150	55	[66]
MoS_2–MoP/FPC	Not applicable	Hydrothermal method	144	41	[67]
N@$MoPC_x$-800	0.14	Polyoxometalate-assisted method	108	69	[68]

the electrocatalyst surface [50].

The EIS was also employed to analyze the impedance of the as-prepared electrocatalysts (Fig. 6(c)). The charge transfer resistance (R_{ct}) of Mo_2C–xNi$(NO_3)_2$/CFP gradually decreased with the increasing of x. When x = 3 M, the R_{ct} of Mo_2C–3 M Ni$(NO_3)_2$/CFP was determined to have the lowest impedance of 5 Ω, which can be attributed to the conductive matrix of CFP and the strong electron donation from Ni to Mo_2C. The R_{ct} of Mo_2C–3.5 M Ni$(NO_3)_2$/CFP (10.5 Ω) and Mo_2C–4 M Ni$(NO_3)_2$/CFP (11.6 Ω) manifests that the overdoping of Ni (x exceeds 3 M) can hinder the process of electron transfer in HER.

To evaluate the ECSA, the double-layer capacitance (C_{dl}) of the samples (Fig. 6(d)) was derived from CV with various scan rates (Fig. S3 in the ESM). The C_{dl} of Mo_2C/CFP is very low (4.8 mF·cm^{-2}). By gradually doping Ni in the catalysts, the C_{dl} of Mo_2C–xNi$(NO_3)_2$/CFP reached the highest value of 73.5 mF·cm^{-2} when x = 3 M, which can be credited to the flower-like Mo_2C clusters induced by Ni doping. Further increasing the x value leads to smaller C_{dl} values, as listed in Table 1. These data are consistent with the morphological observations in Section 3.1.

Long-term durability is a vital criterion for evaluating the HER performance of the catalysts. Chronoamperometry measurement was performed at a static current density of −10 mA·cm^{-2} under acid condition to test the stability of Mo_2C–3 M Ni$(NO_3)_2$/CFP. The results in Fig. 7(a) indicate that Mo_2C–3 M Ni$(NO_3)_2$/CFP possessed exceptional stability and stayed functional over 35 h. The crystalline phase compositions and the nanoflower structure of Mo_2C–3 M Ni$(NO_3)_2$/CFP electrocatalyst remained after long-term durability tests (Figs. 7(b) and 7(c)). The EDS mappings (Fig. 7(d)) and TEM images (Fig. 7(e)) show that its element distribution remained uniform, and the lattice retained its integrity. This observation well supports the superior stability of the electrocatalyst.

3.4 DFT calculations

The experimental data have demonstrated that Mo_2C–

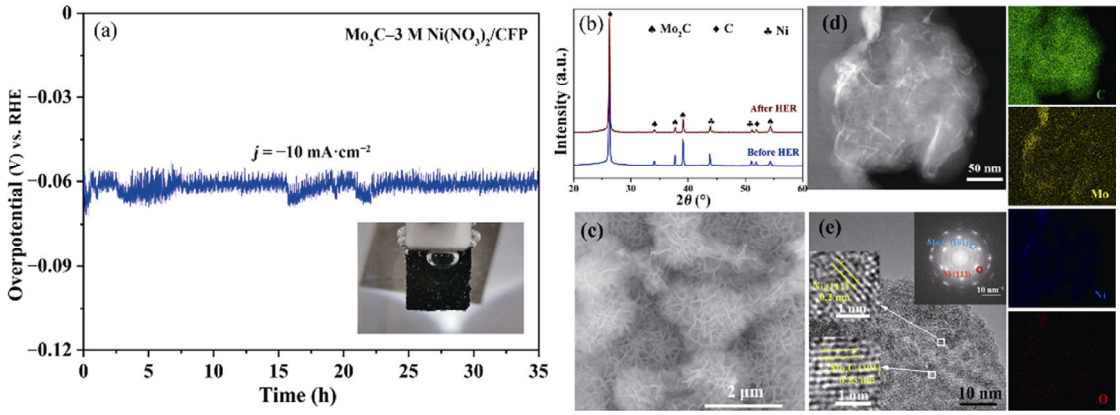

Fig. 7 (a) Stability test for Mo_2C–3 M $Ni(NO_3)_2$/CFP (the inset is a photograph exhibiting the HER process on Mo_2C–3 M $Ni(NO_3)_2$/CFP). (b) XRD pattern, (c) SEM image, (d) EDS mappings, and (e) TEM images of Mo_2C–3 M $Ni(NO_3)_2$/CFP after stability test.

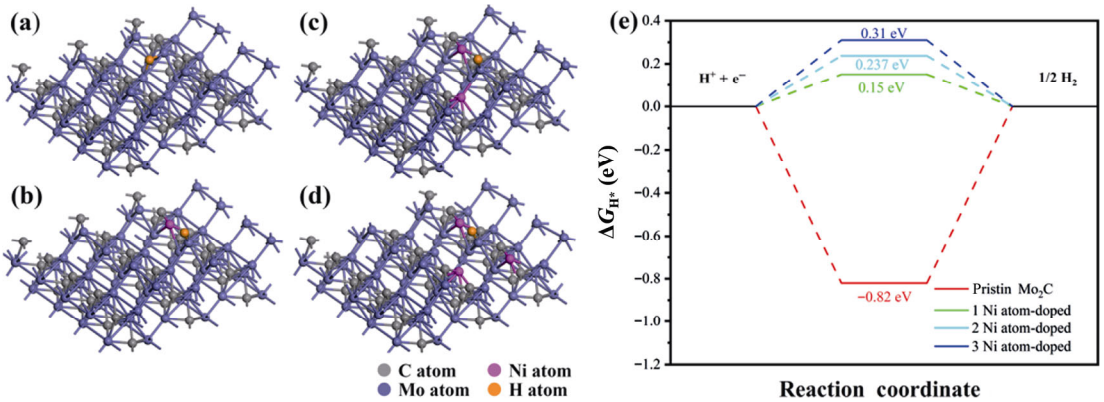

Fig. 8 Theoretical analysis of the mechanism of (a) pristine Mo_2C, (b) 1 Ni atom-doped Mo_2C, (c) 2 Ni atom-doped Mo_2C, (d) 3 Ni atom-doped Mo_2C, and (e) calculated free-energy diagram of H adsorption for HER on the corresponding hybrids.

3 M $Ni(NO_3)_2$/CFP is a very good candidate of HER electrocatalyst with superior catalytic performance, namely highly active, chemically stable, and electrochemically robust. To understand the origin of the excellent catalytic activity, the free energy for hydrogen adsorption (ΔG_{H^*}) was calculated by DFT method, as described in Section 2.5. It is widely accepted that the nearer the ΔG_{H^*} approximates to zero, the more possibility a superior catalyst it may be. For the pristine Mo_2C, ΔG_{H^*} at the surface of (101) lattice plane was calculated to be −0.82 eV, suggesting strong Mo–H bonding on the pristine Mo_2C (Fig. 8). With one Ni atom doped to the structure, the value of ΔG_{H^*} went to 0.15 eV, which was near zero, meaning that Ni doping could facilitate the H_{ads} desorption and lead to faster HER kinetics. However, the ΔG_{H^*} value was calculated to be away from zero when more Ni atoms doped, i.e., 0.237 eV for two Ni atoms doped and 0.31 eV for three ones. DFT calculations illustrate that Ni doping can effectively weaken the Mo–H bonding, thereby improving the HER performance of Mo_2C-based catalysts, while excessive doping would cause adverse effects. Such computational data are in good agreement with the above-discussed electrochemical results. Consequently, the superior HER performance of Mo_2C–3 M $Ni(NO_3)_2$/CFP electrocatalyst can also be attributed to the synergic effect of Ni and Mo_2C.

4 Conclusions

In summary, we developed a self-supporting Ni-doped Mo_2C/CFP electrocatalyst with superior electrocatalytic performance for HER via a one-pot molten salt approach, i.e., soaking MoO_3, CB, and the nickel nitrate solution-pretreated CFP in a chloride molten salt. By gradually increasing the $Ni(NO_3)_2$ concentration from 0 to 3 M, the Ni-doped Mo_2C changed from granular to nanoflower-like morphology with ultra-thin nanosheets. Such morphology significantly enlarged

the ECSA, enriched the active sites, and reduced the impedance within the electrocatalyst. A further higher concentration led to the inhibited electrocatalytic kinetics of the electrocatalyst. The as-developed Mo_2C–3 M $Ni(NO_3)_2$/CFP electrocatalyst is highly active that a small overpotential of 56 mV enabled a current density of 10 $mA \cdot cm^{-2}$, having a fast HER kinetics with a small Tafel slope of 27.4 $mV \cdot dec^{-1}$. Experimental results and DFT calculations lead to the conclusion that the superior HER performance of this electrocatalyst can be attributed to (1) the formation of nanoflower-like morphology (exposing significantly more active sites) and (2) the synergic effect of Ni and Mo_2C not only reducing the HBE and enhancing the electric conductivity, but also facilitating the charge transfer. This work manifests a facile molten salt method to fabricate highly-efficient and robust self-supporting electrocatalysts for water splitting. It further provides a theoretical explanation on the influence of the doping concentration of Ni on the HER performance of the electrocatalysts.

Acknowledgements

This work was financially supported by the National Natural Science Foundation of China (Grant Nos. 51862024, 51772140, and 51962023) and Key Research and Development Program of Jiangxi Province (Grant No. 20203BBE53066).

Electronic Supplementary Material

Supplementary material is available in the online version of this article at https://doi.org/10.1007/s40145-022-0610-6.

References

[1] Liu J, Liu Y, Liu NY, *et al*. Metal-free efficient photocatalyst for stable visible water splitting via a two-electron pathway. *Science* 2015, **347**: 970–974.

[2] Shao YQ, Feng KK, Guo J, *et al*. Electronic structure and enhanced photoelectrocatalytic performance of $Ru_xZn_{1-x}O$/Ti electrodes. *J Adv Ceram* 2021, **10**: 1025–1041.

[3] Chen YJ, Ji SF, Sun WM, *et al*. Engineering the atomic interface with single platinum atoms for enhanced photocatalytic hydrogen production. *Angew Chem Int Ed* 2020, **59**: 1295–1301.

[4] Yang WY, Chen Y, Gao S, *et al*. Post-illumination activity of Bi_2WO_6 in the dark from the photocatalytic "memory" effect. *J Adv Ceram* 2021, **10**: 355–367.

[5] Lin LX, Sherrell P, Liu YQ, *et al*. Engineered 2D transition metal dichalcogenides—A vision of viable hydrogen evolution reaction catalysis. *Adv Energy Mater* 2020, **10**: 1903870.

[6] Xiao P, Sk MA, Thia L, *et al*. Molybdenum phosphide as an efficient electrocatalyst for the hydrogen evolution reaction. *Energy Environ Sci* 2014, **7**: 2624–2629.

[7] Chen ZY, Wang QC, Zhang XB, *et al*. N-doped defective carbon with trace Co for efficient rechargeable liquid electrolyte-/all-solid-state Zn–air batteries. *Sci Bull* 2018, **63**: 548–555.

[8] Chen MZ, Jia YM, Li HM, *et al*. Enhanced pyrocatalysis of the pyroelectric $BiFeO_3$/g-C_3N_4 heterostructure for dye decomposition driven by cold–hot temperature alternation. *J Adv Ceram* 2021, **10**: 338–346.

[9] Gong M, Zhou W, Tsai MC, *et al*. Nanoscale nickel oxide/nickel heterostructures for active hydrogen evolution electrocatalysis. *Nat Commun* 2014, **5**: 4695.

[10] Tang C, Cheng NY, Pu ZH, *et al*. NiSe nanowire film supported on nickel foam: An efficient and stable 3D bifunctional electrode for full water splitting. *Angew Chem Int Ed* 2015, **54**: 9351–9355.

[11] Fu YS, Li J, Li JG. Photo-improved hydrogen evolution reaction activity of the Pt/CdS electrocatalyst. *Prog Nat Sci Mater Int* 2019, **29**: 379–383.

[12] Sugawara Y, Kamata K, Yamaguchi T. Extremely active hydrogen evolution catalyst electrochemically generated from a ruthenium-based perovskite-type precursor. *ACS Appl Energy Mater* 2019, **2**: 956–960.

[13] Zhang J, Chen ZL, Liu C, *et al*. Hierarchical iridium-based multimetallic alloy with double-core–shell architecture for efficient overall water splitting. *Sci China Mater* 2020, **63**: 249–257.

[14] Zou XX, Zhang Y. Noble metal-free hydrogen evolution catalysts for water splitting. *Chem Soc Rev* 2015, **44**: 5148–5180.

[15] Yu ZJ, Mao KW, Feng Y. Single-source-precursor synthesis of porous W-containing SiC-based nanocomposites as hydrogen evolution reaction electrocatalysts. *J Adv Ceram* 2021, **10**: 1338–1349.

[16] Li AL, Sun YM, Yao TT, *et al*. Earth-abundant transition-metal-based electrocatalysts for water electrolysis to produce renewable hydrogen. *Chem-Eur J* 2018, **24**: 18334–18355.

[17] Yu F, Yu L, Mishra IK, *et al*. Recent developments in earth-abundant and non-noble electrocatalysts for water electrolysis. *Mater Today Phys* 2018, **7**: 121–138.

[18] Huang JW, Hong WT, Li J, *et al*. High-performance tungsten carbide electrocatalysts for the hydrogen evolution reaction. *Sustainable Energy Fuels* 2020, **4**: 1078–1083.

[19] Kou ZK, Xi K, Pu ZH, *et al*. Constructing carbon-cohered high-index (222) faceted tantalum carbide nanocrystals as a robust hydrogen evolution catalyst. *Nano Energy* 2017, **36**: 374–380.

[20] Liao L, Wang SN, Xiao JJ, *et al*. A nanoporous

molybdenum carbide nanowire as an electrocatalyst for hydrogen evolution reaction. *Energy Environ Sci* 2014, **7**: 387–392.

[21] Wang WW, Yang L, Chen J, *et al*. Realizing electronic modulation on Mo sites for efficient hydrogen evolution reaction. *J Mater Chem A* 2020, **8**: 18180–18187.

[22] Wu SF, Chen MY, Wang WW, *et al*. Molybdenum carbide nanoparticles assembling in diverse heteroatoms doped carbon matrix as efficient hydrogen evolution electrocatalysts in acidic and alkaline medium. *Carbon* 2021, **171**: 385–394.

[23] Chen MY, Yang DR, Wu SF, *et al*. Self-supporting atmosphere-assisted synthesis of 1D Mo_2C-based catalyst for efficient hydrogen evolution. *Chem-Eur J* 2021, **27**: 9866–9875.

[24] Hou CX, Wang J, Du W, *et al*. One-pot synthesized molybdenum dioxide–molybdenum carbide heterostructures coupled with 3D holey carbon nanosheets for highly efficient and ultrastable cycling lithium-ion storage. *J Mater Chem A* 2019, **7**: 13460–13472.

[25] Wan J, Liu QP, Wang TT, *et al*. Theoretical investigation of platinum-like catalysts of molybdenum carbides for hydrogen evolution reaction. *Solid State Commun* 2018, **284–286**: 25–30.

[26] Chen WF, Wang CH, Sasaki K, *et al*. Highly active and durable nanostructured molybdenum carbide electrocatalysts for hydrogen production. *Energy Environ Sci* 2013, **6**: 943–951.

[27] Kwak WJ, Lau KC, Shin CD, *et al*. A Mo_2C/carbon nanotube composite cathode for lithium–oxygen batteries with high energy efficiency and long cycle life. *ACS Nano* 2015, **9**: 4129–4137.

[28] Yu ZY, Duan Y, Gao MR, *et al*. A one-dimensional porous carbon-supported Ni/Mo_2C dual catalyst for efficient water splitting. *Chem Sci* 2017, **8**: 968–973.

[29] Ma L, Ting LRL, Molinari V, *et al*. Efficient hydrogen evolution reaction catalyzed by molybdenum carbide and molybdenum nitride nanocatalysts synthesized via the urea glass route. *J Mater Chem A* 2015, **3**: 8361–8368.

[30] Xiao P, Yan Y, Ge XM, *et al*. Investigation of molybdenum carbide nano-rod as an efficient and durable electrocatalyst for hydrogen evolution in acidic and alkaline media. *Appl Catal B Environ* 2014, **154–155**: 232–237.

[31] Jing SY, Zhang LS, Luo L, *et al*. N-doped porous molybdenum carbide nanobelts as efficient catalysts for hydrogen evolution reaction. *Appl Catal B Environ* 2018, **224**: 533–540.

[32] Alhajri NS, Anjum DH, Takanabe K. Molybdenum carbide–carbon nanocomposites synthesized from a reactive template for electrochemical hydrogen evolution. *J Mater Chem A* 2014, **2**: 10548–10556.

[33] Liang CH, Ying PL, Li C. Nanostructured β-Mo_2C prepared by carbothermal hydrogen reduction on ultrahigh surface area carbon material. *Chem Mater* 2002, **14**: 3148–3151.

[34] Yang J, Zhang FJ, Wang X, *et al*. Porous molybdenum phosphide nano-octahedrons derived from confined phosphorization in UIO-66 for efficient hydrogen evolution. *Angew Chem Int Ed* 2016, **55**: 12854–12858.

[35] Mo ZY, Yang WY, Gao S, *et al*. Efficient oxygen reduction reaction by a highly porous, nitrogen-doped carbon sphere electrocatalyst through space confinement effect in nanopores. *J Adv Ceram* 2021, **10**: 714–728.

[36] Ang HX, Tan HT, Luo ZM, *et al*. Hydrophilic nitrogen and sulfur co-doped molybdenum carbide nanosheets for electrochemical hydrogen evolution. *Small* 2015, **11**: 6278–6284.

[37] Xiong K, Li L, Zhang L, *et al*. Ni-doped Mo_2C nanowires supported on Ni foam as a binder-free electrode for enhancing the hydrogen evolution performance. *J Mater Chem A* 2015, **3**: 1863–1867.

[38] Yu FY, Gao Y, Lang ZL, *et al*. Electrocatalytic performance of ultrasmall Mo_2C affected by different transition metal dopants in hydrogen evolution reaction. *Nanoscale* 2018, **10**: 6080–6087.

[39] Ouyang T, Chen AN, He ZZ, *et al*. Rational design of atomically dispersed nickel active sites in β-Mo_2C for the hydrogen evolution reaction at all pH values. *Chem Commun* 2018, **54**: 9901–9904.

[40] Hu ZH, Huang JT, Luo Y, *et al*. Wrinkled Ni-doped Mo_2C coating on carbon fiber paper: An advanced electrocatalyst prepared by molten-salt method for hydrogen evolution reaction. *Electrochimica Acta* 2019, **319**: 293–301.

[41] Kresse G, Furthmüller J. Efficient iterative schemes for *ab initio* total-energy calculations using a plane-wave basis set. *Phys Rev B Condens Matter* 1996, **54**: 11169–11186.

[42] Hohenberg P, Kohn W. Inhomogeneous electron gas. *Phys Rev* 1964, **136**: B864–B871.

[43] Kohn W, Sham LJ. Self-consistent equations including exchange and correlation effects. *Phys Rev* 1965, **140**: A1133–A1138.

[44] Blöchl PE. Projector augmented-wave method. *Phys Rev B* 1994, **50**: 17953–17979.

[45] Perdew JP, Burke K, Ernzerhof M. Generalized gradient approximation made simple. *Phys Rev Lett* 1996, **77**: 3865–3868.

[46] Monkhorst HJ, Pack JD. Special points for Brillouin-zone integrations. *Phys Rev B* 1976, **13**: 5188–5192.

[47] Sun JH, Zhu MX, Fan MM, *et al*. Mo_2C–Ni modified carbon microfibers as an effective electrocatalyst for hydrogen evolution reaction in acidic solution. *J Colloid Interface Sci* 2019, **543**: 300–306.

[48] Ou G, Wu FC, Huang K, *et al*. Boosting the electrocatalytic water oxidation performance of $CoFe_2O_4$ nanoparticles by surface defect engineering. *ACS Appl Mater Interfaces* 2019, **11**: 3978–3983.

[49] Arandiyan H, Mofarah SS, Sorrell CC, *et al*. Defect engineering of oxide perovskites for catalysis and energy storage: Synthesis of chemistry and materials science. *Chem Soc Rev* 2021, **50**: 10116–10211.

[50] Zhu YP, Guo CX, Zheng Y, *et al*. Surface and interface engineering of noble-metal-free electrocatalysts for efficient energy conversion processes. *Accounts Chem Res* 2017, **50**: 915–923.

[51] Dong J, Wu Q, Huang CP, *et al*. Cost effective Mo rich Mo_2C electrocatalysts for the hydrogen evolution reaction. *J Mater Chem A* 2018, **6**: 10028–10035.

[52] Vrubel H, Hu XL. Molybdenum boride and carbide catalyze hydrogen evolution in both acidic and basic solutions. *Angew Chem Int Ed* 2012, **51**: 12703–12706.

[53] Li MX, Zhu Y, Wang HY, *et al*. Ni strongly coupled with Mo_2C encapsulated in nitrogen-doped carbon nanofibers as robust bifunctional catalyst for overall water splitting. *Adv Energy Mater* 2019, **9**: 1803185.

[54] Zhao N, Fan HQ, Zhang MC, *et al*. Facile preparation of Ni-doped $MnCO_3$ materials with controlled morphology for high-performance supercapacitor electrodes. *Ceram Int* 2019, **45**: 5266–5275.

[55] Tang Q, Jiang DE. Mechanism of hydrogen evolution reaction on 1T-MoS_2 from first principles. *ACS Catal* 2016, **6**: 4953–4961.

[56] Wang P, Qi J, Chen XZ, *et al*. New insights into high-valence state Mo in molybdenum carbide nanobelts for hydrogen evolution reaction. *Int J Hydrogen Energ* 2017, **42**: 10880–10890.

[57] Zhou Z, Yuan ZW, Li S, *et al*. Big to small: Ultrafine Mo_2C particles derived from giant polyoxomolybdate clusters for hydrogen evolution reaction. *Small* 2019, **15**: 1900358.

[58] Ji LL, Wang JY, Teng X, *et al*. N,P-doped molybdenum carbide nanofibers for efficient hydrogen production. *ACS Appl Mater Interfaces* 2018, **10**: 14632–14640.

[59] Chen L, Jiang H, Jiang HB, *et al*. Mo-based ultrasmall nanoparticles on hierarchical carbon nanosheets for superior lithium ion storage and hydrogen generation catalysis. *Adv Energy Mater* 2017, **7**: 1602782.

[60] Zhang X, Zhou F, Pan WY, *et al*. General construction of molybdenum-based nanowire arrays for pH-universal hydrogen evolution electrocatalysis. *Adv Funct Mater* 2018, **28**: 1804600.

[61] Shi ZP, Nie KQ, Shao ZJ, *et al*. Phosphorus–Mo_2C@carbon nanowires toward efficient electrochemical hydrogen evolution: Composition, structural and electronic regulation. *Energy Environ Sci* 2017, **10**: 1262–1271.

[62] Deng J, Li HB, Wang SH, *et al*. Multiscale structural and electronic control of molybdenum disulfide foam for highly efficient hydrogen production. *Nat Commun* 2017, **8**: 14430.

[63] Wang YL, Senthil RA, Pan JQ, *et al*. Facile construction of N-doped Mo_2C@CNT composites with 3D nanospherical structures as an efficient electrocatalyst for hydrogen evolution reaction. *Ionics* 2019, **25**: 4273–4283.

[64] Yan HJ, Xie Y, Jiao YQ, *et al*. Holey reduced graphene oxide coupled with an Mo_2N–Mo_2C heterojunction for efficient hydrogen evolution. *Adv Mater* 2018, **30**: 1704156.

[65] Hussain S, Vikraman D, Akbar K, *et al*. Fabrication of $MoSe_2$ decorated three-dimensional graphene composites structure as a highly stable electrocatalyst for improved hydrogen evolution reaction. *Renew Energ* 2019, **143**: 1659–1669.

[66] Dong J, Wu Q, Huang CP, *et al*. Cost effective Mo rich Mo_2C electrocatalysts for the hydrogen evolution reaction. *J Mater Chem A* 2018, **6**: 10028–10035.

[67] Zhou QS, Feng JR, Peng XW, *et al*. Porous carbon coupled with an interlaced MoP–MoS_2 heterojunction hybrid for efficient hydrogen evolution reaction. *J Energy Chem* 2020, **45**: 45–51.

[68] Huang YC, Ge JX, Hu J, *et al*. Nitrogen-doped porous molybdenum carbide and phosphide hybrids on a carbon matrix as highly effective electrocatalysts for the hydrogen evolution reaction. *Adv Energy Mater* 2018, **8**: 1701601.